Effect of Cr, Ti, V, and Zr Micro-additions on Microstructure and Mechanical Properties of the Al-Si-Cu-Mg Cast Alloy

S.K. SHAHA, F. CZERWINSKI, W. KASPRZAK, J. FRIEDMAN, and D.L. CHEN

Uniaxial static and cyclic tests were used to assess the role of Cr, Ti, V, and Zr additions on properties of the Al-7Si-1Cu-0.5Mg (wt pct) alloy in as-cast and T6 heat-treated conditions. The microstructure of the as-cast alloy consisted of α-Al, eutectic Si, and Cu-, Mg-, and Fe-rich phases $Al_{2.1}Cu$, $Al_{8.5}Si_{2.4}Cu$, $Al_{5.2}CuMg_4Si_{5.1}$, and $Al_{14}Si_{7.1}FeMg_{3.3}$. In addition, the micro-sized Cr/Zr/Ti/V-rich phases $Al_{10.7}SiTi_{3.6}$, $Al_{6.7}Si_{1.2}TiZr_{1.8}$, $Al_{21.4}Si_{3.4}Ti_{4.7}VZr_{1.8}$, $Al_{18.5}Si_{7.3}Cr_{2.6}V$, $Al_{7.9}Si_{8.5}Cr_{6.8}V_{4.1}Ti$, $Al_{6.3}Si_{23.2}FeCr_{9.2}V_{1.6}Ti_{1.3}$, $Al_{92.2}Si_{16.7}Fe_{7.6}Cr_{8.3}V_{1.8}$, and $Al_{8.2}Si_{30.1}Fe_{1.6}Cr_{18.8}V_{3.3}Ti_{2.9}Zr$ were present. During solution treatment, Cu-rich phases were completely dissolved, while the eutectic silicon, Fe-, and Cr/Zr/Ti/V-rich intermetallics experienced only partial dissolution. Micro-additions of Cr, Zr, Ti, and V positively affected the alloy strength. The modified alloy in the T6 temper during uniaxial tensile tests exhibited yield strength of 289 MPa and ultimate tensile strength of 342 MPa, being significantly higher than that for the Al-Si-Cu-Mg base. Besides, the cyclic yield stress of the modified alloy in the T6 state increased by 23 pct over that of the base alloy. The fatigue life of the modified alloy was substantially longer than that of the base alloy tested using the same parameters. The role of Cr, Ti, V, and Zr containing phases in controlling the alloy fracture during static and cyclic loading is discussed.

I. INTRODUCTION

THE recent growth in use of lightweight materials in automotive manufacturing is an answer to rising fuel costs as automakers try to provide consumers with greater fuel efficiency to meet stringent Corporate Average Fuel Efficiency (CAFE) regulations. The purpose of using light metals is to reduce the vehicle weight, increase fuel economy, improve vehicle performance, and enhance overall safety.[1–3] Due to low density, high specific strength and stiffness, and good recyclability, aluminum alloys are becoming attractive structural materials in the automotive and aerospace industries.[4,5] So far, applications of existing Al alloys are limited to about 453 K (180 °C).[6] Beyond this temperature, the mechanical properties deteriorate quickly due to precipitates coarsening. To meet the requirements of automotive engine parts, the Al-Si alloys may be modified by changing their chemical composition and post-casting heat treatment.[6,7] Thus, new demands of the automotive industry for aluminum alloys suitable for high-temperature power train applications require the development of cast Al-Si alloys with enhanced thermal stability.

According to Knipling,[8] to develop cast Al alloys for high-temperature applications, alloying elements should fulfill several conditions. In particular, they should (i) be capable of forming thermally stable strengthening phases, (ii) have low solid solubility in the Al matrix, (iii) have low diffusivity in the Al matrix, and (iv) retain the ability for the alloy to be conventionally solidified. It is reported that among alloying elements, transition metals which form thermally stable and coarsening-resistant precipitates are promising in case of Al-Si alloys. A review of the published phase diagrams and crystallographic data[9–12] indicates that a number of alloying additions crystallize to form stable Al_3M-trialuminides. The high-symmetry cubic $L1_2$ and related tetragonal $D0_{22}$ and $D0_{23}$ structures are prevalent among transition elements. To achieve this, different alloying elements such as Ni, Fe, Cr, Ti, V, and Zr were examined with cast Al-Si alloys as described in the literature.[13–30]

Studies[31–33] showed that Al-Si alloys contain a certain amount of Fe impurities, which form β-AlSiFe ($Al_9Si_2Fe_2$) phase. This phase is needle-like in shape and detrimental for alloy properties especially ductility. Modifications of the Fe-rich phase are very common in Al-Si alloys by adding transition metals such as Mn, Ti, V, and Zr. This modification changes the morphology of the phase constituent, improving the alloy properties.[31–33] Recently published data showed that

S.K. SHAHA, Ph.D. Candidate, and J. FRIEDMAN and D.L. CHEN, Professors, are with the Department of Mechanical and Industrial Engineering, Ryerson University, 350 Victoria Street, Toronto, ON M5B 2K3, Canada. F. CZERWINSKI, Group Leader, Research Scientist, is with CanmetMATERIALS, Natural Resources Canada, 183 Longwood Road South, Hamilton, ON L8P 0A1, Canada, and also Adjunct Professor with the Department of Mechanical and Industrial Engineering, Ryerson University. Contact e-mail: frank.czerwinski@nrcan.gc.ca W. KASPRZAK, Director of Operations, is with CanmetMATERIALS, Natural Resources Canada.

additions of Cr in Al-Si alloy also could boost the high-temperature properties, especially tensile strength, by forming dispersoid phases.[26,34] Although studies on strain-controlled low cycle fatigue (LCF) provide important input into the design of machine parts,[35] unfortunately most of the literature data are focused on tensile properties. To the authors' knowledge, the study on the LCF fatigue resistance of cast Al-Si-Cu-Mg alloys for automotive power train applications, in particular the Al-Si-Cu-Mg alloys modified with addition of Cr-Zr-V-Ti is so far not available.

Thus, the aim of this paper is to explore the role of Cr, Zr, Ti, and V additions in the LCF behavior of the Al-Si-Cu-Mg alloy at different strain amplitudes. The fatigue mechanism related to various strain amplitudes under LCF conditions is analyzed in detail and compared with the Al-Si-Cu-Mg base alloy cast using the same parameters.

II. EXPERIMENTAL DETAILS

A. Alloy Casting and Metallography

The experimental alloys were prepared in a 30-kg induction furnace by mixing commercial master alloys of Al-20wt pct-Cr, Al-50wt pctCu, Al-35wt pctSi, Al-6.1wt pctTi, Al-85wt pctV, Al-10wt pctZr, Al-10wt pctSr, and pure metals, Mg and Al to achieve the targeted chemistry, as listed in Table I. To confirm the proper dissolution of intermetallics present in the master alloys, the melt temperature was raised to 1123 K (850 °C). The alloy was cast at 1013 K (740 °C) into a permanent mold made of copper and covered with a water jacket. After pouring the liquid metal, water was circulated through the jacket to achieve the solidification rate of approximately 20 K (°C)/s. After casting, the Al-Si-Cu-Mg-(Cr-Zr, V, Ti) alloy was subjected to T6 heat treatment in an air circulating resistance furnace with an accuracy of ± 5 K (°C). The T6 heat treatment consisted of a two-step solutionizing at 783 K (510 °C) for 0.5 hours and at 798 K (525 °C) for 4.5 hours followed by water quench. After solution treatment, the samples were stored at a temperature of 233 K (-40 °C) for 8 hours followed by artificial aging at 473 K (200 °C) for 1 hour with subsequent air cooling.

For microstructural study, samples were prepared following standard metallographic procedures explained in Reference 32. The microstructure of both alloys was examined in the unetched condition using an optical microscope (OM) and a scanning electron microscope (SEM), equipped with energy-dispersive X-ray spectroscopy (EDS). Details of the identification of the intermetallic phases are explained in Reference 36.

B. Mechanical Testing

Mechanical properties of alloys were evaluated in terms of uniaxial tensile strength and LCF life. The tensile tests were performed at room temperature on as-cast and T6 heat-treated specimens following the ASTM: E8/E8M-11 standard. The tensile samples with a gage length of 25 mm (or parallel length of 32 mm) were extracted from the center of the wedge-shaped casting having secondary dendrite arm spacing (SDAS) of ~25 μm as shown in Reference 3. A computerized universal testing machine was used to determine the alloy properties at a strain rate of 10^{-3} s^{-1}. For each set of tests, at least two samples were used.

For LCF experiments, the strain-controlled pull-push type fatigue tests were conducted using a computerized Instron 8801 fatigue testing system at a zero mean strain (i.e., a strain ratio of $R_s = -1$, completely reversed strain cycle), and at room temperature of 298 K (25 °C). A triangular loading waveform was followed during LCF testing. LCF tests were performed at different strain amplitudes of 0.1, 0.2, 0.3, 0.4, 0.5, and 0.6 pct. At least two samples were tested at each level of strain amplitude. The strain-controlled measurements at lower strain amplitude levels were continued up to 10,000 cycles, considered cyclically stable, then the tests were changed to stress control at a frequency of 50 Hz using the sine cyclic waveform for infinite fatigue life. If the sample survived up to a fatigue cycle of 10^7, then the life cycle was considered as infinite. After tensile and fatigue tests, the fracture surfaces were analyzed using SEM/EDS.

III. RESULTS

A. Microstructure

The microstructures of the modified alloy in the as-cast and T6 heat-treated conditions and the base alloy in the T6 heat-treated condition are shown in Figure 1. Compositions of phases evaluated using EDS along with literature suggestions are given in Table II. Microstructural analysis revealed that the as-cast microstructure of the modified alloy consisted of α-Al dendrites (#1), modified Al-Si eutectic (#2), and twelve distinct intermetallic dispersoid phases, as listed in Table II. The phase identified as Al$_{2.1}$Cu (#3) is most likely related to θ-Al$_2$Cu,[16] while Al$_{8.5}$Si$_{2.4}$Cu (#4) is suggested as Al-Al$_2$Cu-Si ternary eutectic,[37] Al$_{5.2}$Cu Mg$_4$Si$_{5.1}$ (#5) is recommended as Q-Al$_5$Cu$_2$Mg$_8$Si$_6$ phase, and Al$_{14}$Si$_{7.1}$FeMg$_{3.3}$ (#6) is pertinent to one of the Fe-containing, possibly, π-Al$_8$FeMg$_3$Si$_6$ phases. Similar types of phases were found in the Al-Si-Cu-Mg base alloy in the as-cast condition.[16,38–40] The

Table I. The Chemistry of the Base and Modified Al-Si-Cu-Mg Alloy with Addition of Ti, V, Zr, and Cr in Weight Percent

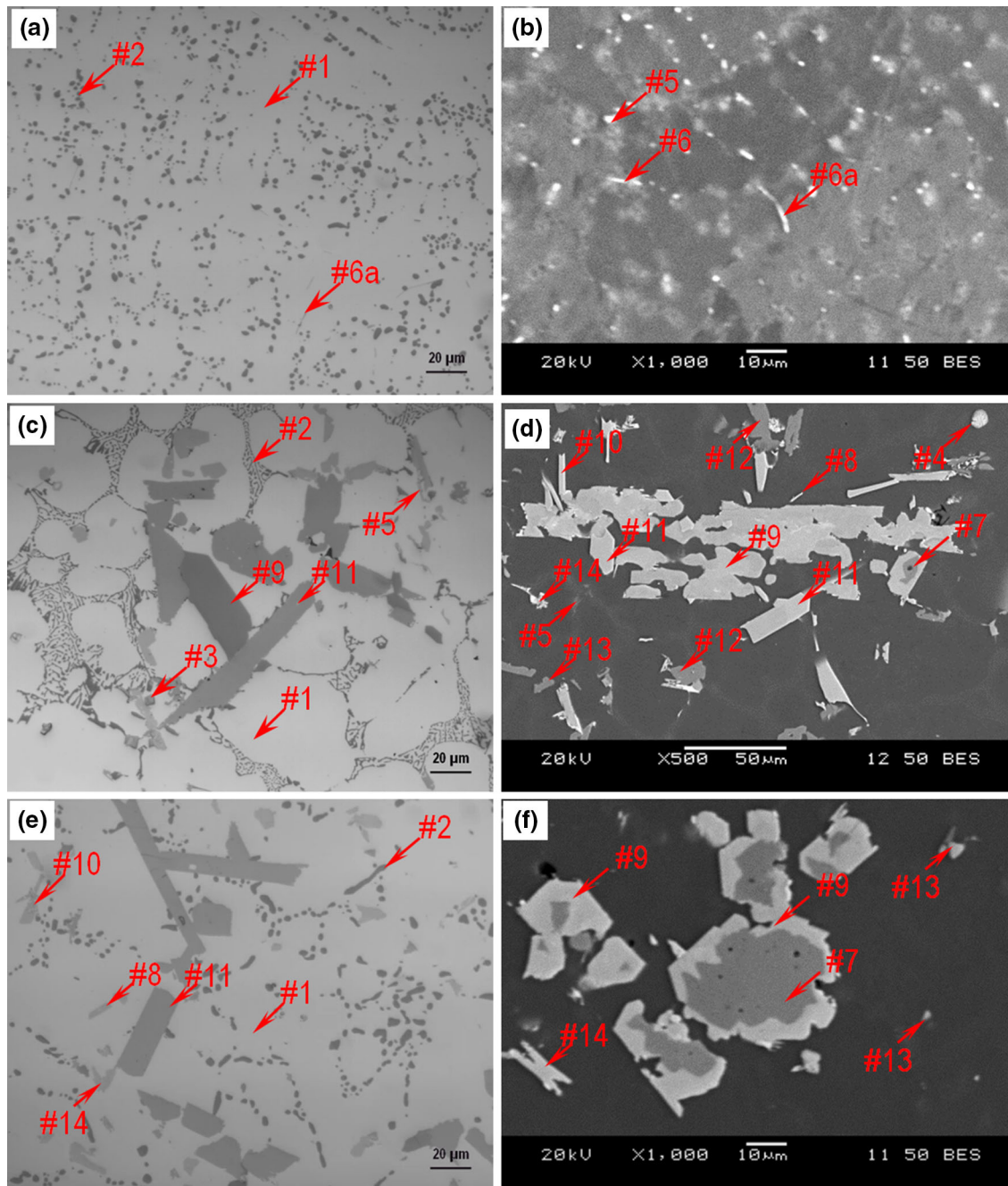| Alloy	Si	Cu	Mg	Fe	Sr	Ti	Zr	V	Cr	Al
Base alloy	0.1	1.0	0.50	—	0.008	—	—	—	—	bal.
Modified alloy	7.0	1.0	0.50	0.12	0.008	0.39	0.25	0.39	0.47	bal.

Fig. 1—OM (*a, c, e*) and SEM (*b, d, f*) microstructures of the cast base (a, b) and modified (c through f) Al-Si-Cu-Mg alloy with addition of Ti, V, Zr, and Cr. Note that numbered arrows correspond to phases are outlined in Table II.

Zr-Ti-V-containing micro-sized phases are found in the as-cast alloy. They are $Al_{10.7}SiTi_{3.6}$ (#7), $Al_{6.7}Si_{1.2}TiZr_{1.8}$ (#8), and $Al_{21.4}Si_{3.4}Ti_{4.7}VZr_{1.8}$ (#9) which were described in the literature as $(AlSi)_3Ti$, $(AlSi)_3(TiZr)$, and $(AlSi)_3(TiVZr)$, respectively.[16,38,41] Other intermetallics were identified as Cr-rich phases. They are $Al_{18.5}Si_{7.3}Cr_{2.6}V$ (#10), and $Al_{7.9}Si_{8.5}Cr_{6.8}V_{4.1}Ti$ (#11) which can be considered as $(AlSi)_3(CrV)$ and $(AlSi)_3(CrVTi)$, respectively, as reported in References 32, 36, 41. The latter phases were found in interdendritic regions and most likely nucleated during last stages of

the alloy solidification process. The detrimental Fe-containing β-Al_5FeSi (#6a) phase was only identified in the base alloy. However, after addition of Cr-Ti-V-Zr to the Al-Si-Cu-Mg alloy, the Fe-containing β-Al_5FeSi phase disappeared. Instead, three distinct phases formed as $Al_{6.3}Si_{23.2}FeCr_{9.2}V_{1.6}Ti_{1.3}$ (#12), $Al_{92.2}Si_{16.7}Fe_{7.6}Cr_{8.3}V_{1.8}$ (#13), and $Al_{8.2}Si_{30.1}Fe_{1.6}Cr_{18.8}V_{3.3}Ti_{2.9}Zr$ (#14). The latter phases could be described as $Al_{13}(FeCrVTi)_4Si_4$, α-$Al_{12}(FeCrV)_3Si$, and $(AlSi)_2$ $(TiZrCr)Fe$, similar to phases reported in References 18, 41.

Table II. The Main Phases Identified Using SEM/EXD in the As-cast Alloy and Their Response During T6 Temper

| No.	Calculated Phase from SEM/EDS Point Analysis	Suggested Phase in the Literature	Response During T6 Temper
#1	α-aluminum	α-aluminum	no change
#2	eutectic silicon	eutectic silicon	partially dissolved/thermally modified
#3	$Al_{2.1}Cu$	Al_2Cu	dissolved
#4	$Al_{8.5}Si_{2.4}Cu$	$Al-Al_2Cu-Si$	dissolved
#5	$Al_{5.2}CuMg_4Si_{5.1}$	$Al_5Cu_2Mg_8Si_6$	partially dissolved
#6	$Al_{14}Si_{7.1}FeMg_{3.3}$	$Al_8FeMg_3Si_6$	partially dissolved
#6a	$Al_{3.4}Fe_{0.1}Si_{0.2}$	$β-Al_5FeSi$	no change
#7	$Al_{10.7}SiTi_{3.6}$	$(AlSi)_3Ti$	no change
#8	$Al_{6.7}Si_{1.2}TiZr_{1.8}$	$(AlSi)_3(TiZr)$	partially dissolved
#9	$Al_{21.4}Si_{3.4}Ti_{4.7}VZr_{1.8}$	$(AlSi)_3(TiVZr)$	no change
#10	$Al_{18.5}Si_{7.3}Cr_{2.6}V$	$(AlSi)_3(CrV)$	partially dissolved
#11	$Al_{7.9}Si_{8.5}Cr_{6.8}V_{4.1}Ti$	$(AlSi)_3(CrVTi)$	no change
#12	$Al_{6.3}Si_{23.2}FeCr_{9.2}V_{1.6}Ti_{1.3}$	$Al_{13}(FeCrVTi)_4Si_4$	no change
#13	$Al_{92.5}Si_{16.7}Fe_{7.6}Cr_{8.3}V_{1.8}$	$α-Al_{12}(FeCrV)_3Si$	partially dissolved
#14	$Al_{8.2}Si_{30.1}Fe_{1.6}Cr_{18.8}V_{3.3}Ti_{2.9}Zr$	$(AlSi)_2(TiZrCr)Fe$	no change

(a)

(b)
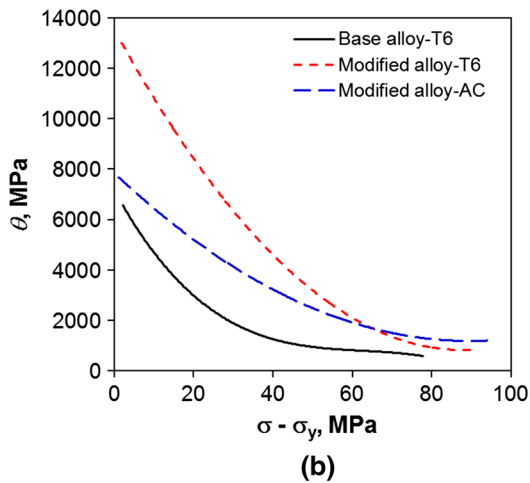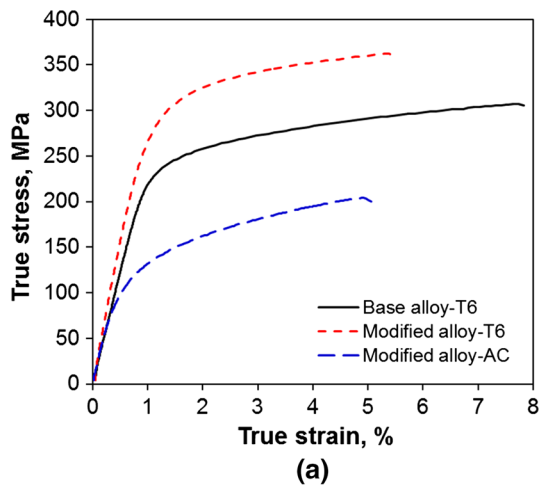
Fig. 2—A comparison between base and modified alloy (*a*) stress–strain curves (*b*) and K–M plot of the base and modified Al-Si-Cu-Mg alloy with addition of Ti, V, Zr, and Cr during tensile loading.

The microstructural analysis of the T6 heat-treated samples confirmed that the Cu-containing phases (#3 and #4) were completely dissolved in the modified alloy

(Figures 1(c) and (d)) and in the base alloy (Figures 1(e) and (f)). At the same time, phases #5 and #6 containing Mg- and Fe-rich phases including eutectic Si partially dissolved in both alloys. In addition, the Fe-containing $β-Al_5FeSi$ (#6a) phase in the base alloy remained unchanged. Other phases present in the modified alloy, containing Cr, Ti, V, and Zr, #8, #10, and #13 were partially dissolved during solution treatment (Figures 1(c) and (d)). In contrast, phases #7, #9, #11, #12, and #14 were retained in an unchanged condition after T6 temper, which indicates their thermal stability at elevated temperatures. It should be noted that phase #7 was surrounded by phase #9. It is believed that phases (#7-#14) formed as a result of additions of Cr-, Ti-, V-, and Zr-into the base alloy during melting and solidification. Similar phases were described in previous studies.[18,41]

B. Mechanical Properties

1. Stress–strain behavior during tensile loading

The true stress–true strain plot of the modified and base alloys in as-cast and T6 heat-treated conditions tested at room temperature is shown in Figure 2(a). The as-cast modified alloy achieved a yield strength (YS) of 112 MPa, an ultimate tensile strength (UTS) of 179 MPa, and an elongation of 3.54 pct. It is seen that the T6 heat treatment improved significantly the alloy properties. The T6 heat-treated modified alloy shows YS of 289 MPa and UTS of 342 MPa with higher ductility of 3.82 pct. In contrast, the base alloy in the T6 heat-treated condition achieved a substantially lower YS of 230 MPa and UTS of 301 MPa with a higher ductility of 6.45 pct. The test concludes that the modified alloy shows improved UTS and YS, but lower ductility compared to the base alloy.

The UTS and ductility are essential parameters characterizing the alloy quality. As described in References 42, 43, the quality index (Q_{index}) of both alloys was calculated and listed in Table III. The calculated Q_{index} for the modified alloy in the T6 heat-treated condition is

Table III. Tensile Properties of the Base and Modified Al-Si-Cu-Mg Alloy with Addition of Ti, V, Zr, and Cr, Tested at a Strain Rate of 1×10^{-3} s^{-1}

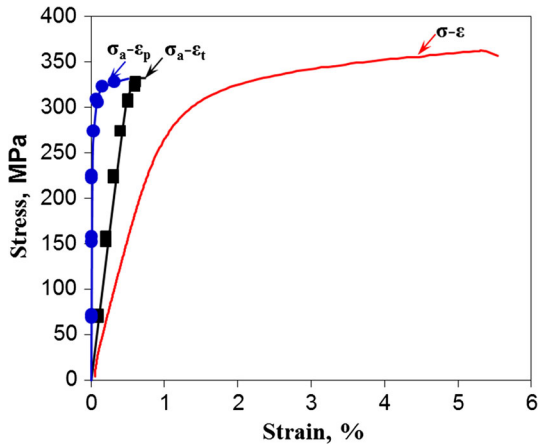| Alloy	Alloys State	YS, (MPa)	US, (MPa)	E, (pct)	HC	n	Q_{index}, (MPa)
Modified	AC	112	179	3.54	0.60	0.31	246
	T6	289	342	3.82	0.19	0.13	423
Base	T6	230	301	6.45	0.31	0.15	418

Fig. 3—Stress–strain curves obtained during different loading conditions tension and cyclic loading at a strain rate.

higher than that for the base alloy. It is noticed that the modified alloy in the as-cast state obtained a Q_{index} value of ~246 MPa, whereas the modified alloy in the T6 state gained higher Q_{index} of ~423 MPa. In contrast, the base alloy in the T6 state shows lower Q_{index} value of ~418 MPa. Thus, it can be concluded that the alloy modified with additions of Cr-Ti-Zr-V in T6 state obtained better tensile properties than the Al-Si-Cu-Mg base.

The work-hardening behavior of alloys is revealed through the plot of the instantaneous work-hardening rate of $\theta = d\sigma/d\varepsilon$ vs net flow stress increments of $\sigma - \sigma_y$, referred to as the Kocks–Mecking (K–M) plot.[44] The stages of work-hardening described by Kocks–Mecking, known as stages II, III, and IV characterize the linear hardening, falling of hardening rate, and finally the saturation. The hardening stages III and IV are generally seen in polycrystalline materials during tensile loading.[44,45] As depicted in Figure 2(b), the work-hardening rate revealed only the hardening stages III and IV. The nature of the curves indicates that the modified alloy in the T6 heat-treated condition achieved a higher hardening rate compared to the same alloy in the as-cast state and the base alloy after T6 heat treatment. At the beginning of stage III, the forest dislocation hardening occurred due to the dislocations interaction, their accumulation, and dynamic recovery, which caused a linear reduction of the hardening rate.

Work-hardening, which affects the alloy mechanical properties, relies on the generation and annihilation of

dislocations during deformation.[46,47] Hereafter, the hardening capacity, which can be expressed by the following equation, is defined as the ability to create and store dislocations in materials,[48,49]

$$H_c = \frac{\sigma_{\text{UTS}} - \sigma_Y}{\sigma_Y} = \frac{\sigma_{\text{UTS}}}{\sigma_Y} - 1, \qquad [1]$$

where H_c is the hardening capacity, σ_{UTS} is the ultimate tensile strength, and σ_Y is the yield strength. The calculated value of the hardening capacity is given in Table III. It is clear that due to the T6 temper, the hardening capacity of the modified alloy decreased from 0.60 to 0.19 while the base alloy shows a H_c value of 0.31. It is seen that the hardening capacity of the modified alloy is lower than that for the base alloy. However, it is similar to values reported for 319-T6 and 356-T6 alloys.[48] Normally, when a material is strengthened, the YS increases while the hardening capability increases due to higher storage capacity of dislocations during plastic deformation.[49] This is mainly attributed to higher YS and US, and lower ductility of the modified alloy. As the modified alloy has lower ductility and lower plastic deformation, it results in reduced storage of dislocations leading to the lower hardening capacity. However, the presence of porosity and detrimental needle-shaped phases causes a reduction of tensile properties of the base alloy.

Another parameter describing the plastic deformation is the work-hardening exponent n. It can be evaluated from the true stress–true strain curves, as seen in Figure 2(a). The work-hardening exponent n and strength coefficient K can be evaluated from Hollomon's equation:

$$\sigma = K\varepsilon^n, \qquad [2]$$

where σ is the true flow stress, and ε is the corresponding true strain.

The work-hardening exponent n is calculated from the uniform plastic deformation region between the YS point and the UTS point. The as-cast modified alloy exhibited a work-hardening exponent of 0.31 during tension, while for the T6 temper state, work-hardening in tension decreased to 0.13. In contrast, the base alloy revealed the work-hardening exponent of 0.15. The n value of the T6 temper sample is in agreement with that reported in Reference 50 for A356-T6 alloy where $n \approx 0.17$ was obtained. The strain hardening exponent was also reported to be strongly dependent on the aging temperature for A356-T6 alloy with n values ranging from 0.08 to 0.17.[48,51]

Table IV. Low Cycle Fatigue Parameters for the Cast T6 Base and Modified Al-Si-Cu-Mg Alloy with Addition of Ti, V, Zr, and Cr

Low Cycle Fatigue Parameters	Base Alloy	Modified Alloy in T6 State
Cyclic yield strength, σ'_y, MPa	265	327
Cyclic strain hardening exponent, n'	0.14	0.10
Cyclic strength coefficient, K', MPa	630	639
Fatigue strength coefficient, σ'_y, MPa	285	427
Fatigue strength exponent, b	−0.03	−0.09
Fatigue ductility coefficient, ε'_f , pct	0.30	2.35
Fatigue ductility exponent, c	−0.25	−0.82
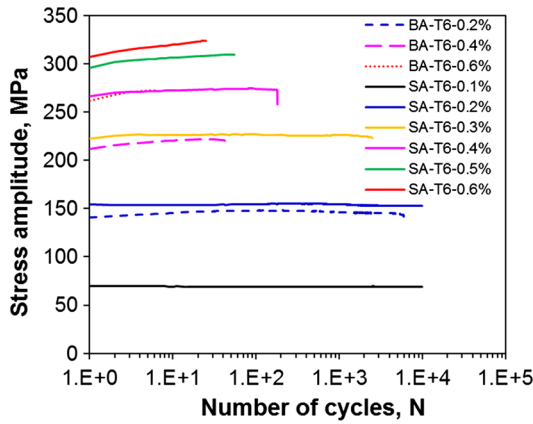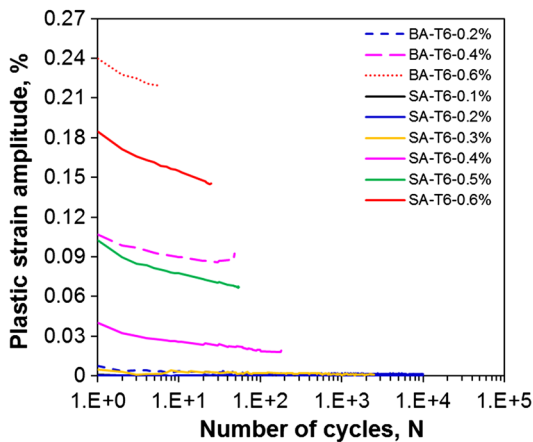
Fig. 4—Plot of (*a*) cyclic stress amplitudes *vs* the number of cycles, and (*b*) cyclic plastic strain amplitudes *vs* the number of cycles during the strain-controlled low cycle fatigue tests for T6 heat-treated alloys. Note: BA-base alloy, SA-studied alloy.

2. Stress–strain behavior during LCF loading

The LCF stress–strain ($\sigma_a - \Delta\varepsilon_t/2$) curves of the modified alloy in the T6 temper condition are shown in Figure 3. In this equation, σ_a is the stress amplitude at midlife and $\Delta\varepsilon_t$ is the total strain range. This figure also shows the plot of stress amplitude at midlife and the corresponding plastic strain amplitude. The corresponding tensile true stress–strain plot is also given as a comparison. Thus, the modified alloy showed higher hardening behavior during cyclic loading as compared to tensile loading. It is also evident that the alloy did not

show any plastic deformation at lower strain amplitudes from 0.1 to 0.3 pct. However, with increasing strain amplitude from 0.4 to 0.6 pct, the alloy exhibited noticeable plastic deformation. To assess precisely the work-hardening behavior of the T6 temper samples, the cyclic stress–strain parameters were characterized by exploring Hollomon's relationship,[23,35,52]

$$\frac{\Delta\sigma}{2} = K'\left(\frac{\Delta\varepsilon_p}{2}\right)^{n'}, \qquad [3]$$

where $\Delta\sigma/2$ is the stress amplitude at midlife and $\Delta\varepsilon_p/2$ is the corresponding plastic strain amplitude, n' is the cyclic work-hardening exponent, and K' is the cyclic strength coefficient.

The evaluated cyclic work-hardening exponent and cyclic strength coefficient are listed in Table IV for the modified and base alloys. It is seen that both the n' and K' values for the modified alloy of $n' = 0.10$ and $K' = 639$ MPa are lower than those for the base alloy ($n' = 0.28$ and $K' = 2393$ MPa) and the A356-T6 alloy ($n' = 0.24$ and $K' = 1628$ MPa) reported in Reference 50. However, the strength coefficient of the base alloy ($K' = 639$ MPa) is lower and the work-hardening exponent ($n' = 0.14$) is higher than that for the modified alloy. Also, the evaluated cyclic yield strength of the modified alloy in the T6 temper is 327 MPa, which is higher than the tensile yield strength (Table III). It is also seen that the higher cyclic yield strength of the modified alloy increased by ~23 pct as compared to the base alloy (265 MPa). It is suggested that the alloys in the present study have a stronger hardening capability under LCF loading than under tensile loading. Similar results were reported by other researchers during monotonic and cyclic deformations of Al-Si alloys.[35,48,50]

3. Low cycle fatigue life of the alloy

The behavior of cyclic stress amplitude as a function of the number of cycles at different total strain amplitudes during LCF tests is shown in Figure 4(a) for both the modified and base alloys in the T6 temper condition. The experimental curves show similar trends for both alloys. In general, there is an increase in stress amplitude and a decrease in fatigue life with applied total strain amplitude. At lower total strain amplitudes (0.1 to 0.3 pct), the cyclic stress amplitude remained nearly constant throughout the entire fatigue life. At higher total strain amplitudes from 0.5 to 0.6 pct, cyclic hardening occurred from the beginning and continued
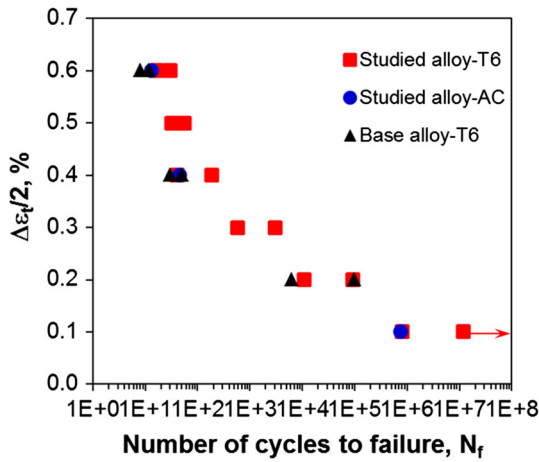
Fig. 5—Fatigue life of Al-Si-Cu-Mg alloy with addition of Ti, V, Zr, and Cr in as-cast and T6 heat-treated condition in comparison with the base alloy, obtained at total strain amplitudes of 0.1 to 0.6 pct.

up to failure for the T6 tempered samples as cyclic deformation proceeded. However, at 0.4 pct total strain amplitude, at the beginning, the alloy showed cyclic hardening with increasing total stress amplitude up to ~8 cycles followed by nearly constant total stress amplitude for all fatigue life cycles. The cyclic hardening tendency became stronger with increasing strain amplitudes from 0.5 to 0.6 pct, as indicated by steeper slope in the semi-log scale diagram (Figure 4(a)). The cyclic deformation characteristics occurring in the modified alloy (σ_{YS} = ~289 MPa, Table III) are in agreement with data reported in References 32, 48, 50 for Al-Si alloys.

Another change was observed through curves of cyclic stress amplitude as a function of the number of cycles at different total strain amplitudes. The initial cyclic stress amplitudes increased from ~70 to ~304 MPa with increasing the total strain amplitude from 0.1 to 0.6 pct, respectively. Compared to the base alloy, the modified alloy experienced higher initial cyclic stress amplitude for the samples tested above 0.1 pct total strain amplitudes. The cyclic hardening behavior of the modified alloy is related to its YS. If the total stress amplitude is much lower than the YS, the alloy will not undergo cyclic hardening and plastic deformation. As seen in Figure 4(a), at lower strain amplitudes (0.1 to 0.3 pct), the maximum total stress amplitude is much lower (~70 to ~220 MPa) than the YS (289 MPa), while at higher total strain amplitudes (0.4 to 0.6 pct), the maximum total stress amplitude was much closer (~265 to ~304 MPa) to the YS (289 MPa) of the modified alloy. Therefore, at lower strain amplitudes, the studied alloy does not experience any hardening, while at higher strain amplitudes the hardening occurred throughout the entire fatigue life.

Figure 4(b) shows the plastic strain amplitude as a function of the number of cycles for both the base and modified alloys in the T6 temper condition. As the total strain amplitude increased, the plastic strain amplitude also increased with decreasing fatigue life of the alloy. At higher strain amplitudes (0.4 to 0.6 pct), the plastic
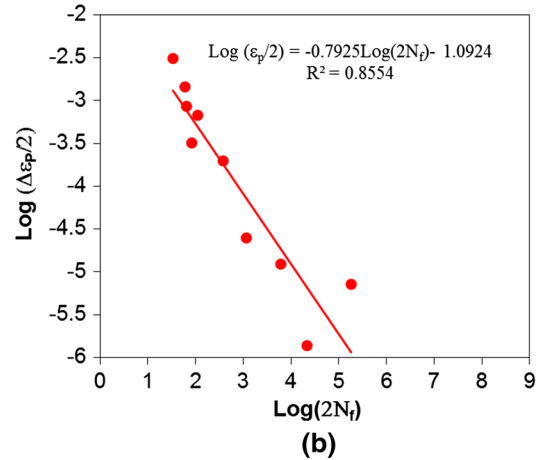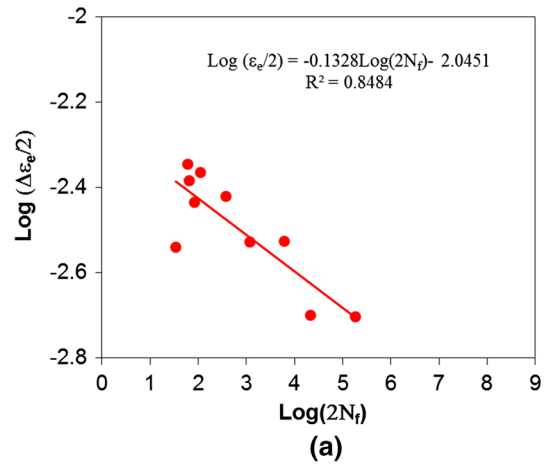

Fig. 6—Plot of fatigue-tested data of Al-Si-Cu-Mg alloy with addition of Ti, V, Zr, and Cr in T6 heat-treated condition; (a) Basquin plot and (b) Coffin–Manson plot.

strain amplitude of the modified alloy decreased almost linearly until failure, while it remained almost constant at lower total strain amplitudes of 0.1 to 0.3 pct. In contrast, the base alloy attained higher plastic stress amplitude for the samples tested above 0.3 pct total strain amplitudes. This corresponds well to the cyclic hardening and stability characteristics seen in Figure 4(a) at the same total strain amplitude.

Figure 5 shows the fatigue lifetime curves known as strain *vs* the number of cycles to failure (generally ε-N curves) for the modified and base alloys in the T6 tempered condition. The plot reveals that the fatigue life increased with decreasing total strain amplitude for both alloys. The fatigue life of the modified alloy seemed significantly longer than the base alloy at all levels of total strain amplitudes. Moreover, the fatigue data of cast alloys exhibited a fairly large scatter due to the microstructural inhomogeneity, especially the type and size of casting defects,[53,54] which will be discussed later. The improved fatigue resistance of the modified alloy is mainly attributed to the composite-like strengthening and presence of dispersoid phases that became active upon introducing Cr-Zr-Ti-V alloying elements to the base alloy.
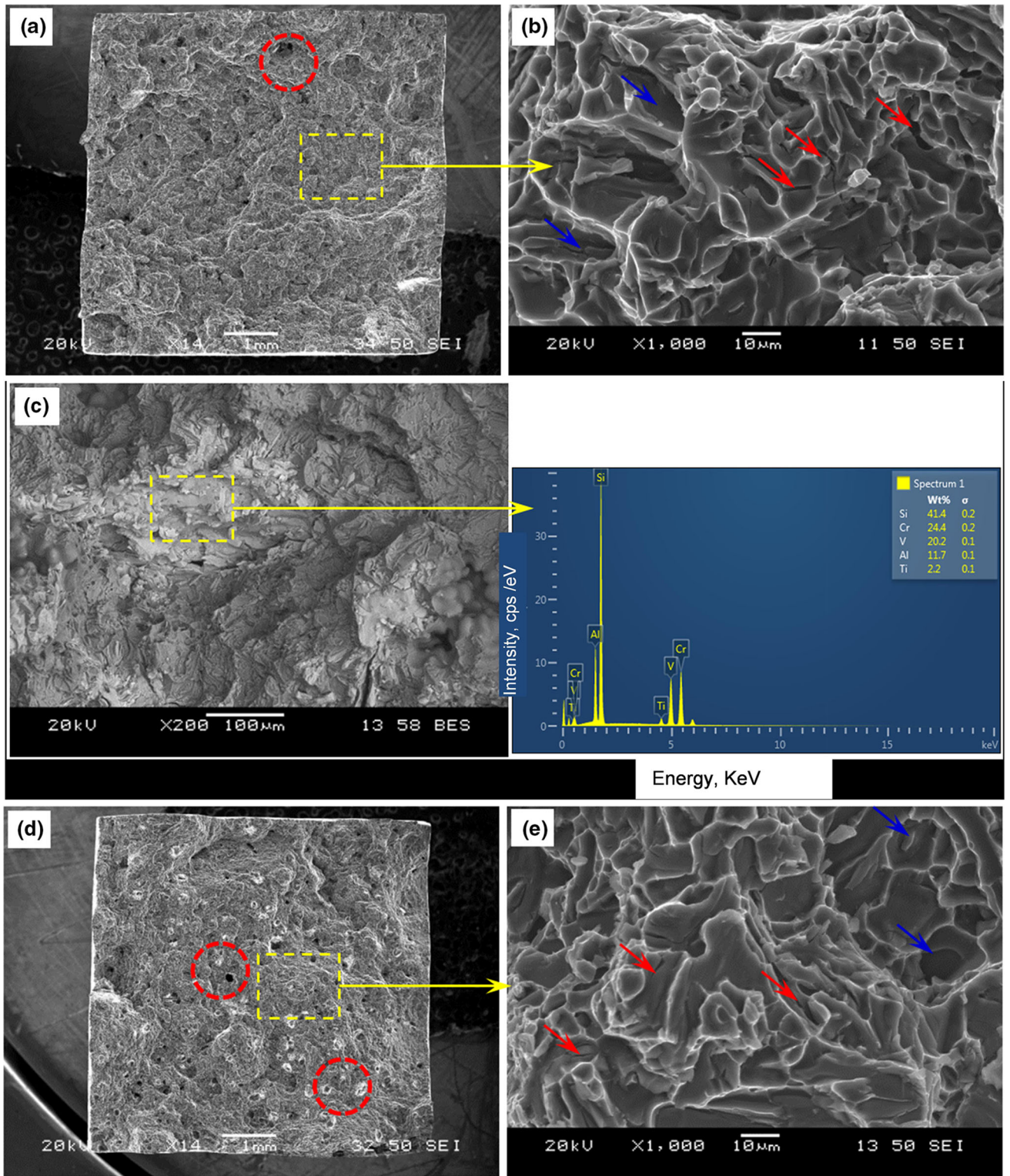
Fig. 7—SEM image of the tensile fracture surface of modified (*a*, *b*, and *c*) and the base (*d*, *e*) Al-Si-Cu-Mg alloy with addition of Ti, V, Zr, and Cr in T6 heat-treated condition. The EDS spectrum in Fig. 7(c) shows chemical composition of the area indicated on the fracture surface.

During LCF, the total strain amplitude is a combination of the elastic strain amplitude and the plastic strain amplitude as shown in the following equation[35,51]:

$$\frac{\Delta\varepsilon_t}{2} = \frac{\Delta\varepsilon_e}{2} + \frac{\Delta\varepsilon_p}{2},$$
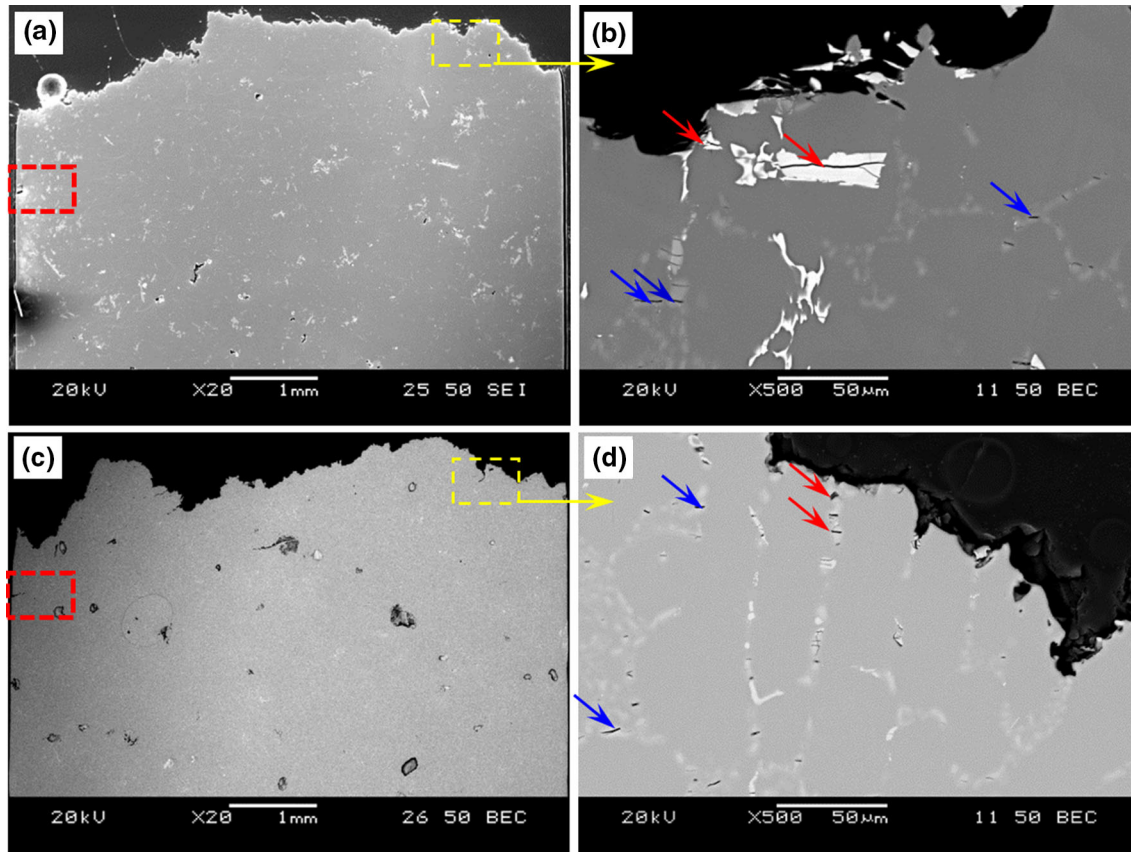
[4]

Fig. 8—SEM microstructure of the modified (*a, b*) and base (*c, d*) Al-Si-Cu-Mg alloy with addition of Ti, V, Zr, and Cr in T6 tempered condition after tension test as observed on polished cross section, (a, c) overall view and (b, d) magnified view as enclosed by yellow box in (a, c) (Color figure online).

where $\frac{\Delta\varepsilon_t}{2}$ is the total elastic strain amplitude, $\frac{\Delta\varepsilon_e}{2}$ is the elastic strain amplitude, and $\frac{\Delta\varepsilon_p}{2}$ is the plastic strain amplitude.

The relationship between the elastic strain amplitude and the number of reversals of fatigue life ($2N_f$) can be characterized by the Basquin equation as follows[48,51]:

$$\frac{\Delta\varepsilon_e}{2} = \frac{\sigma'_f}{E}(2N_f)^b, \qquad [5]$$

where E is Young's modulus, N_f is the number of cycles to failure, σ'_f is the fatigue strength coefficient, and b is the fatigue strength exponent.

Also, the relationship between the plastic strain amplitude and the number of reversals of fatigue life ($2N_f$) can be denoted by Coffin–Manson's equation as follows[48,51]:

$$\frac{\Delta\varepsilon_p}{2} = \varepsilon'_f(2N_f)^c, \qquad [6]$$

where ε'_f is the fatigue ductility coefficient and c is the fatigue ductility exponent.

By combining both Eqs. [5] and [6], the fatigue life can be estimated using the following relationship known as Coffin–Manson–Basquin's.[51]

$$\frac{\Delta\varepsilon_t}{2} = \frac{\Delta\varepsilon_e}{2} + \frac{\Delta\varepsilon_p}{2} = \frac{\sigma'_f}{E}(2N_f)^b + \varepsilon'_f(2N_f)^c. \qquad [7]$$

In the present study, the values of elastic or plastic strain amplitudes are taken at half-life from the hysteresis loops of each alloy considering the stable condition of the LCF. As seen in Figure 6, the log–log plot of Eqs. [5] and [6] were used to calculate the fatigue design parameters. The values of the above parameters were evaluated following linear regression and are provided in Table IV http://www.sciencedirect.com/science/article/pii/S0921509314001610-t0015 for the modified and base alloys.[48] The results indicate that the fatigue strength coefficient and the fatigue strength exponent significantly increased to 427 MPa and ~0.09, respectively, in the modified alloy. As compared with the base alloy in the same condition, the fatigue ductility coefficient and exponent of the modified alloy increased significantly from 0.30 to 2.35 pct and from −0.25 to −0.82. Thus, it could be concluded that the modified alloy has significantly better fatigue properties compared to the base alloy.

C. Fractography

1. Fractography of the tensile tested samples

A general view of selected base and modified alloys in the T6 temper condition fractured after tension testing is shown in Figure 7. It is a common feature that the ductile fracture begins by forming voids due to cracking of the second-phase particles. When the critical stress

exceeded the interfacial bonding between the matrix and the particles, the particle cracking occurred, resulting in the formation of voids in the matrix. However, casting defects such as internal pores, dry oxide, and shrinkage, are also susceptible places for crack nucleation.

Fractographic observations revealed that the fracture characteristics were most likely similar for the modified and base alloys. The fracture surface after tensile loading exhibited mostly intergranular features along with some fragmentation of the Cr-Zr-Ti-V-rich intermetallics as identified by EDS analysis (Figure 7(c)). In addition, open pores were present on the tensile fracture surface, as marked by red circle in Figures 7(a) and (d). Some eutectic silicon particles were de-bonded from the matrix as pointed out by blue arrow, which was accompanied by secondary cracks between dendrites, marked by red arrows in Figures 7(b) and (e). Such morphology suggests that there was a strong interaction between the plastic flow or slip bands and the eutectic silicon particles especially at grain boundaries leading to initiation of intergranular cracking. Similar types of fracture behavior were also noted by others for the Al-Si-Cu-Mg alloy with additions of Zr, Ti, and V during tensile loading.[21,32,48]

As discovered by SEM analysis on polished cross sections of the T6 tempered alloys after tension testing (Figure 8(a)), the secondary cracking and small amounts of plastic deformation occurred near the fracture surface, which is indicated by the red box in Figures 8(a) and (c). Also, micro-cracking occurred mainly within the eutectic silicon particles as pointed out by blue arrows in conjunction with the Cr-Zr-Ti-V-rich intermetallics, as indicated by red arrows in Figure 8(b). In contrast, the base alloy exhibited micro-cracking in the Fe-rich β-Al$_5$FeSi intermetallics (Figure 8(d)). Multiple cracks were found mainly in the high-aspect ratio particles, due to the fact that there is a strong interfacial bonding between the aluminum matrix and the particles. Occasionally, debonding between the particle and matrix was also observed. However, the direction of cracks developed in the eutectic silicon and intermetallic particles after tension was perpendicular to the loading axis (Figures 8(b) and (d)). Similar behavior of the intermetallics during tensile loading was identified in our previous studies.[21,32]

2. Fractography of the alloy after cyclic loading

Figure 9 shows SEM images of the fatigue crack initiation site and propagation zone for both the base and modified alloys tested at 0.2 pct total strain amplitude. Since at 0.2 pct total strain amplitude all samples experience failure, these samples were considered as failed at the lowest strain amplitude and used for fractographic analysis.

As reported in Reference 32, three distinct zones can be identified on the fracture surface after LCF testing; i.e., (i) fatigue crack initiation (FCI) zone, (ii) fatigue crack growth/propagation (FCG) zone, and (iii) final fracture zone which is adjacent to the uneven FCG zone. It is seen that the size of the propagation zone indicated by red dashed line in Figure 9(a) is larger for the modified alloy (Figure 9(c)). The highly magnified

images in Figures 9(b) and (d) showed that the crack initiation in both alloys occurred from the casting defects near the sample surface, such as large surface pores or oxide layers. These sites acted as stress concentrators that initiated the formation of fatigue cracks.[50,55,56] The location enclosed in a white box on the fracture surface in Figure 9, was further magnified in Figures 10(a) through (d), revealing detailed features of cracking. It is clear that the crack propagation zone of the base alloy in Figure 10(a) appeared different from the modified alloy tested at higher strain amplitude of 0.2 pct (Figure 10(c)). As shown in Figure 10(a), coarse fatigue striations, which are surrounded by tear ridges of grain boundaries, are obvious on fracture surfaces of the base alloy tested at a strain amplitude of 0.2 pct. In contrast, the modified alloy developed fine fatigue striations, which are also surrounded by tear ridges of grain boundaries (Figure 10(c)). The micro-cliffs have a step-like pattern formed inside of the grain parallel to the FCG path, which seem to indicate lateral slippage at the crack tip.[35,57] For the modified alloy (Figure 10(c)), however, the fatigue striation spacing (FSS) seemed relatively fine while for the base alloy, it is comparatively coarse, (Figure 10(a)). This phenomenon suggests that the extent of increase of total strain amplitude is the key to determine the fatigue striation characteristics of the Al-Si alloys. As observed in face-centered cubic materials, fatigue striations are normally generated via a repeated plastic blunting–sharpening process due to the slip of dislocations in the plastic zone in front of the fatigue crack tip.[58] As the material exhausted the final stage of fatigue crack propagation, the remaining volume was not strong enough to withstand the applied stress/strain. As a result, the crack advanced mainly through the eutectic Si, creating a non-flat appearance and tensile-like features in the final rapid fracture, as shown in Figures 10(b) and (d) which is very similar to the static tensile fracture surface shown previously in Figures 7(b) and (e) Similar features of LCF fracture in cast aluminum alloys were observed by other researchers.[35,48,50]

IV. DISCUSSION

A. Analysis of Microstructure

The Al-Si-Cu-Mg base alloy forms a complex microstructure as stated previously.[39,40,59] Additions of transition metals of Cr-Zr-Ti-V made this microstructure even more complex. There are limited studies on cast Al-Si-Cu-Mg alloys with addition of transition metals, in particular Cr-Zr-Ti-V, which could be used as a direct reference. The closest ones are our studies involving Ti, Zr, and V additions.[32,36,41] Thus, the key difference is Cr, absent there. Recently, Hernandez-Sanoval et al.[16] modified the Al-Si-Cu-Mg alloy with minor additions of Ti, Zr, and Ni, where they reported a variety of phases bearing Zr and Ti.

The microstructural complexity of the Al-Si-Cu-Mg alloy containing Cr, Zr, V, and Ti is confirmed in Figure 1. The phase identified as Al$_{2.1}$Cu (Figure 1(b)) is
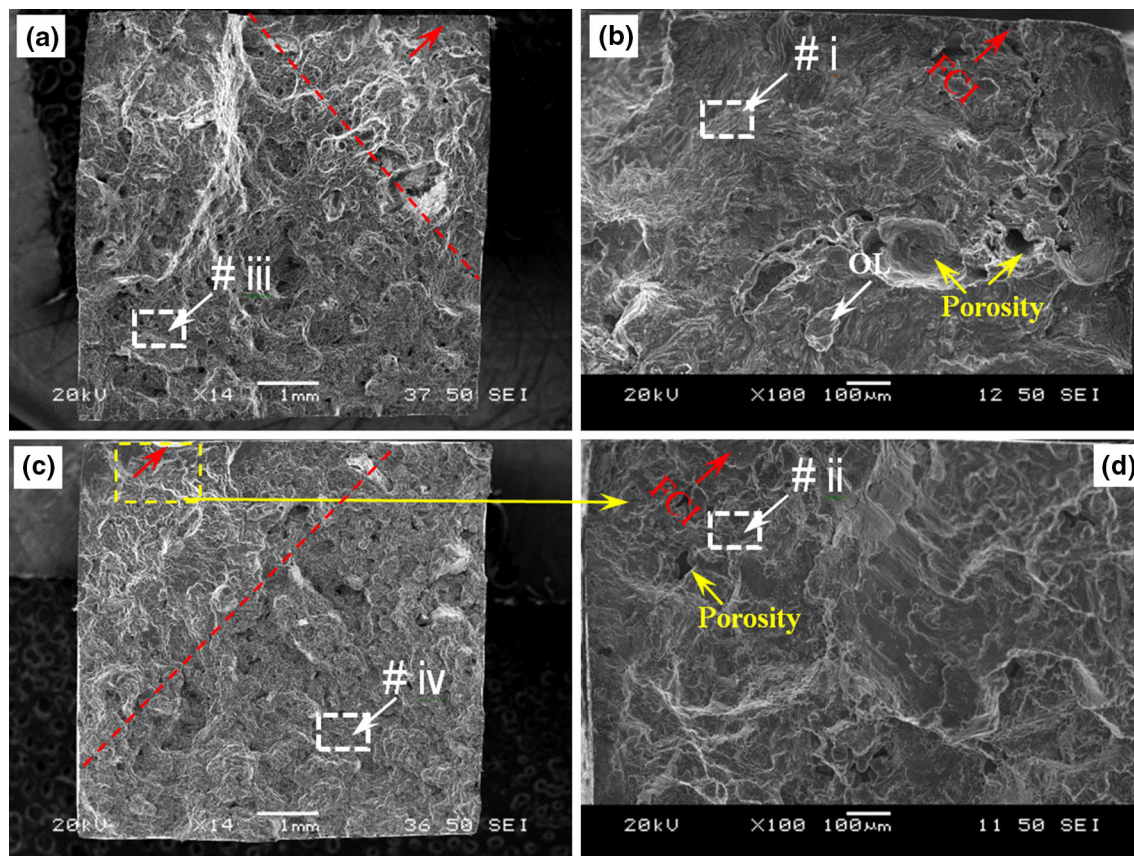
Fig. 9—SEM images of fatigue fracture surfaces of the samples tested at a total strain amplitude of 0.2 pct showing an overall view (*a*, *c*) for T6 heat-treated base (a, b) and modified (c, d) Al-Si-Cu-Mg alloy with addition of Ti, V, Zr, and Cr with the corresponding fatigue crack initiation sites at higher magnifications, where fatigue cracks initiate at a large surface pore (b); clusters of near-surface pores and large surface inclusion (d). Here, yellow box and red arrows indicate the position of crack initiation sites while red dashed line separated the crack propagation area. Note that the modified alloy has larger crack propagation zone compared to the base alloy (Color figure online).

most likely related to the Al_2Cu compound, reported in the literature. The $Al_{8.5}Si_{2.4}Cu$ phase is similar to the ternary eutectic $Al-Al_2Cu-Si$, the $Al_{5.2}CuMg_4Si_{5.1}$ phase is similar to the $Q-Al_5Cu_2Mg_8Si_6$ phase, and the $Al_{14}Si_{7.1}FeMg_{3.3}$ phase is most likely recognized as the Fe-rich $Al_8FeMg_3Si_6$ phase that is typically formed in the base alloy. Additionally, the $Al_{3.4}Fe_{0.1}Si_{0.2}$ phase identified in the base alloy can be considered as $\beta-Al_5FeSi$, which is similar to the phase present in the Al-Si-Cu-Mg cast alloy systems.[16,38,60]

A review of phase diagrams and crystallographic data[9,11,12] indicates that a number of alloying additions crystallize to form stable Al_3M-trialuminides. The high-symmetry cubic $L1_2$ and related tetragonal $D0_{22}$ and $D0_{23}$ structures are prevalent among transition elements. The Al_3M has three types of crystallographic structure. They are metastable $L1_2$ and $D0_{22}$ phases, and the stable $D0_{23}$ phase containing Ti/V/Zr.[10] The observed Ti- and Zr-Ti-rich intermetallic phases, $Al_{10.7}SiTi_{3.6}$ and $Al_{6.7}Si_{1.2}TiZr_{1.8}$ in the as-cast microstructure could be associated with the crystal structure of $Al_3M/(D0_{23})$[10,61] and the suggested formulas $(AlSi)_3(Ti)$ and $(AlSi)_3(TiZr)$, respectively. Similar compounds were detected in the Al-Si-Cu-Mg alloy with the addition of the Ti, V, and Zr.[32] Another Zr/Ti/V-rich intermetallic phase is $Al_{21.4}Si_{3.4}Ti_{4.7}VZr_{1.8}$ that can be summarized as $(AlSi)_3(TiVZr)$.[18,36,41] The crystal structure of the first phase is $D0_{22}$ while the crystal structure of the latter two phases can be interrelated with the stable phase $D0_{23}$. Although the Zr content in the investigated alloy was above the peritectic concentration of 0.15 pct (Table I), the pre-peritectic primary Al_3M (M = Zr/V/Ti) phase was not formed as a stand-alone compound.

Other intermetallic phases present in the modified alloy were formed due to additions of Cr-Zr-Ti-V. The obtained Cr-V-rich and Cr-Ti-V-rich intermetallic phases, $Al_{18.5}Si_{7.3}Cr_{2.6}V$ and $Al_{7.9}Si_{8.5}Cr_{6.8}V_{4.1}Ti$ can be associated with the crystal structure of $Al_3M/(D0_{23})$. Gao and Liu[30] showed that Zr/V/Ti can replace each other in the Al_3M structure. It seems that Cr can also replace the Zr/V/Ti and form Cr-V-rich and Cr-Ti-V-rich intermetallic phases which can be expressed as $(AlSi)_3(CrV)$ and $(AlSi)_3(CrVTi)$. It should be pointed out that there was not the iron-containing needle-like $\beta-Al_5FeSi$ phase in the modified alloy. Instead, three intermetallics containing Fe were formed. They are plate-shaped $Al_{13}(FeCrVTi)_4Si_4$, and bulk-shaped $\alpha-Al_{12}(FeCrV)_3Si$ and $(AlSi)_2(TiZrCr)Fe$ phases which are similar to phases reported in References 26, 34. Since these phases bond Fe, they contribute to improvement in alloy mechanical properties.
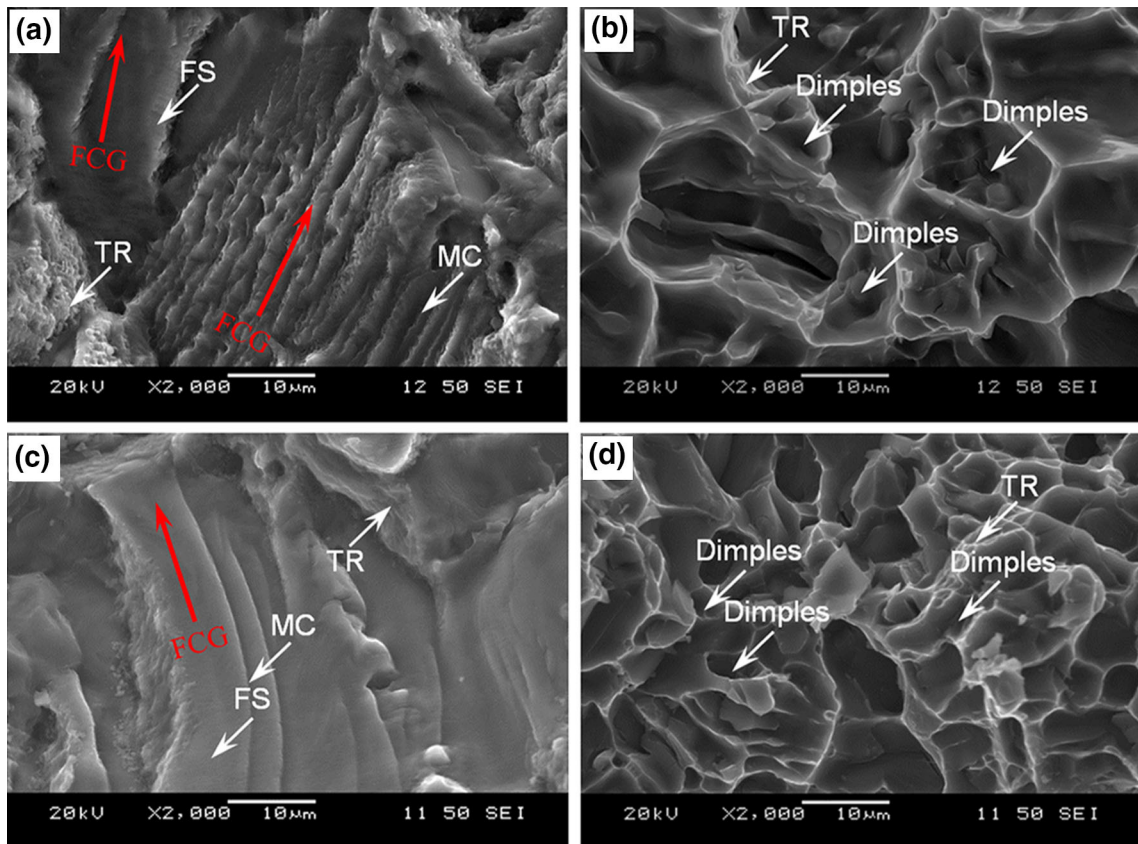
Fig. 10—SEM images of fatigue fracture surfaces of the T6 heat-treated samples of base (*a*, *b*) and modified (*c*, *d*) Al-Si-Cu-Mg alloy with addition of Ti, V, Zr, and Cr tested at a strain amplitude of 0.2 pct showing fatigue striation in matrix (a, c) (as indicated by white box in Figs. 9(b) and (d) with i and ii) and (b, d) final fracture (as pointed out in Figs. 9(a) and (c) with iii and iv). Note: FCG-fatigue crack growth, FS-fatigue striation, MC-micro-cliff, and TR-tear ridge.

The easy dissolution of Cu-containing phases was confirmed by SEM and EDS analysis of both alloys in the T6 heat-treated condition. It was also revealed that the Fe-rich phase partially dissolved and changed its morphology. As reported in Reference 41, the Fe-rich phase present in the as-cast Al-Si-Cu-Mg alloy transformed after T6 heat treatment into two distinct Fe-rich phases containing Cu or Mg *i.e.*, $Al_9Mg_{12}Si_6Fe$ and AlSiCuFe phases. This study shows that Cr/Zr/Ti/V-rich intermetallic phases with different morphologies (#7, #9, #11, #12, and #14) with stable crystal structure remained after T6 heat treatment. However, some phases like #8, #10, and #13 were partially dissolved. During solution treatment, the partial dissolution of these intermetallics increases concentrations of Cr, Zr, Ti, and V solutes, which are available for secondary precipitation in the matrix. During aging, formation of these precipitates reduces the amount of solute, and its quantity in the solid solution depends on heat treatment parameters.[18,41]

B. *Modification of Mechanical Properties*

The evaluated mechanical properties show that additions of Cr, Zr, Ti, and V to the Al-Si-Cu-Mg alloy achieved higher tensile properties compared to the base composition. The observed improvement is associated with the modification of alloy microstructure and the presence of trialuminide dispersoid phases, as reported in References 20, 41. The significant enhancement of UTS is attributed to the composite-like role of Cu-, Fe-, and Mg-containing intermetallics, modification of eutectic-Si particles (Figure 1), and the precipitation strengthening by nano-sized trialuminide particles, which are uniformly distributed in the aluminum matrix.[38,40,48,50] These dispersoid intermetallics effectively hinder the movement of dislocations during tensile loading resulting in an improvement of the alloy strength (Table III). Also, the presence of trialuminide precipitates restricts the grain growth during T6 heat treatment at the stage of solutionizing. As a result, the grain refinement strengthening positively contributes to the alloy performance. Additions of Cr change the morphology of the Fe-bearing phase which essentially improves the alloy tensile properties.

The LCF test results of the modified alloy showed better properties than that of the base alloy. The obtained cyclic YS was higher than the monotonic YS which indicates the higher hardening and better dislocation storage capacity during cyclic loading. It is seen that the base alloy in the T6 condition has 62 MPa lower cyclic YS, as compared to the modified alloy. At the same time, the modified alloy has significantly higher (~8 times) fatigue ductility coefficient, which leads to longer

fatigue life. It seems that morphological changes of Fe-rich intermetallics and eutectic Si enhanced the alloy fatigue life. The initiation, propagation and growth of fatigue cracks is controlled by casting defects such as gas porosity or dry oxide and microstructural features such as SDAS and morphology of dispersoid intermetallics.[53,56] Especially pores, which are open to surface, are prone to nucleate cracks as seen in Figures 9(a) and (c). It was previously confirmed that fatigue cracks preferentially initiate at pores or voids and inclusions during cyclic deformation.[35,48,62] Also, needle-like β-Al_5FeSi precipitates enhance the stress concentration around them, which accelerates the fatigue crack growth, consequently reducing the fatigue life of the base alloy. In contrast, the modified alloy contains Fe-bearing intermetallics and Cr-rich phases that improve the alloy strength and fatigue life.

V. CONCLUSIONS

The uniaxial tensile and low cycle fatigue properties of the Al-Si-Cu-Mg alloy modified with additions of Cr, Ti, V, and Zr were investigated. On the basis of the microstructure, stress–strain characteristics and low cycle fatigue behavior, the following conclusions can be drawn:

The Al-Si-Cu-Mg alloy with additions of Cr, Zr, Ti, and V developed a complex microstructure, which in the as-cast state was composed of α-Al, eutectic Si, and Cu, Mg, and Fe-based phases $Al_{2.1}Cu$, $Al_{8.5}Si_{2.4}Cu$, $Al_{5.2}CuMg_4Si_{5.1}$, and $Al_{14}Si_{7.1}FeMg_{3.3}$. In addition, microsized Cr/Zr/Ti/V-rich phases, $Al_{10.7}SiTi_{3.6}$, $Al_{6.7}Si_{1.2}TiZr_{1.8}$, $Al_{21.4}Si_{3.4}Ti_{4.7}VZr_{1.8}$, $Al_{18.5}Si_{7.3}Cr_{2.6}V$, $Al_{7.9}Si_{8.5}Cr_{6.8}V_{4.1}Ti$, $Al_{6.3}Si_{23.2}FeCr_{9.2}V_{1.6}Ti_{1.3}$, $Al_{92.2}Si_{16.7}Fe_{7.6}Cr_{8.3}V_{1.8}$, and $Al_{8.2}Si_{30.1}Fe_{1.6}Cr_{18.8}V_{3.3}Ti_{2.9}Zr$ were identified in the as-cast state. The solutionizing treatment during T6 temper completely dissolved the Cu-based $Al_{2.1}Cu$ and $Al_{8.5}Si_{2.4}Cu$ phases while the $Al_{5.2}CuMg_4Si_{5.1}$, $Al_{14}Si_{7.1}FeMg_{3.3}$, $Al_{6.7}Si_{1.2}TiZr_{1.8}$, $Al_{18.5}Si_{7.3}Cr_{2.6}V$, and $Al_{92.2}Si_{16.7}Fe_{7.6}Cr_{8.3}V_{1.8}$ phases only partially dissolved. In contrast, the $Al_{10.7}SiTi_{3.6}$, $Al_{21.4}Si_{3.4}Ti_{4.7}VZr_{1.8}$, $Al_{7.9}Si_{8.5}Cr_{6.8}V_{4.1}Ti$, $Al_{6.3}Si_{23.2}FeCr_{9.2}V_{1.6}Ti_{1.3}$, $Al_{92.2}Si_{16.7}Fe_{7.6}Cr_{8.3}V_{1.8}$, and $Al_{8.2}Si_{30.1}Fe_{1.6}Cr_{18.8}V_{3.3}Ti_{2.9}Zr$ phases were stable and remained unchanged after T6 heat treatment.

Micro-additions of Cr, Zr, Ti, and V positively affected the Al-Si-Cu-Mg alloy strength. The modified alloy in the T6 temper condition during uniaxial tensile tests exhibited yield strength of 289 MPa and ultimate tensile strength of 342 MPa, significantly higher than that for the Al-Si-Cu-Mg base alloy. The measured ductility of 3.82 pct was lower as compared to the base. The cyclic yield stress of the modified alloy in the T6 temper condition increased by 23 pct over that of the base alloy.

The fatigue life of the modified alloy was substantially longer than that of the base alloy tested using the same parameters. The cyclic stress amplitude and plastic strain amplitude were almost cyclically stable at low total strain amplitudes of 0.1 to 0.4 pct. Cyclic hardening occurred at higher strain amplitudes with the extent of cyclic hardening increasing with increasing the total strain amplitude from 0.5 to 0.6 pct.

The fractographic analysis showed that the tensile cracks propagated mainly through the eutectic Si and primary phases resulting in intergranular fracture. Also, multiple cracking of Cr/Zr/Ti/V-rich dispersoid phases was observed on fracture surfaces. The fatigue cracks were primarily affected by near-surface casting defects like pores and oxide inclusions. The propagation of fatigue crack was characterized by fatigue striations in connection with secondary cracks in the α-Al matrix.

REFERENCES

1. W. Kasprzak, H. Kurita, J.H. Sokolowski, and H. Yamagata: *Adv. Mater. Process.*, 2010, vol. 168, pp. 24–27.
2. R. Tucker: *Met. Finish.*, 2013, vol. 111, pp. 31–33.
3. S.K. Shaha, F. Czerwinski, W. Kasprzak, J. Friedman, and D.L. Chen: *Mater. Sci. Eng. A*, 2015, vol. 636, pp. 361–72.
4. H. Toda, T. Nishimura, K. Uesugi, Y. Suzuki, and M. Kobayashi: *Acta Mater.*, 2010, vol. 58, pp. 2014–25.
5. G. Wang, X. Bian, W. Wang, and J. Zhang: *Mater. Lett.*, 2003, vol. 57, pp. 4083–87.
6. S.K. Das, P.S. Gilman, and D. Raybould: *Key Eng. Mater.*, 1989, vols. 38–39, pp. 367–92.
7. H. Jones: *Materials in Aerospace: Vol. 1*, The Royal Aeronautical Society, London, 1986.
8. K.E. Knipling: *Development of a Nanoscale Precipitation-Strengthened Creep-Resistant Aluminum Alloys Containing Trialuminide Precipitates*, Northwestern University, Evanston, IL, 2006.
9. N.A. Belov, D.G. Eskin, and N.N. Avxentieva: *Acta Mater.*, 2005, vol. 53, pp. 4709–22.
10. T. Sato, A. Kamio, and G.W. Lormier: *Mater. Sci. Forum*, 1996, vols. 217–222, pp. 895–900.
11. V. Raghavan: *J. Phase Equilib. Diffus.*, 2005, vol. 26, pp. 639–40.
12. M. Bulanova, L. Tretyachenko, M. Golovkova, and K. Meleshevich: *J. Phase Equilib. Diffus.*, 2004, vol. 25, pp. 209–29.
13. S.K. Chaudhury and D. Apelian: *Metall. Mater. Trans. A*, 2006, vol. 37A, pp. 763–78.
14. P. Sepehband, R. Mahmudi, and F. Khomamizadeh: *Scripta Mater.*, 2005, vol. 52, pp. 253–57.
15. R. Mahmudi, P. Sepehrband, and H.M. Ghasemi: *Mater. Lett.*, 2006, vol. 60, pp. 2606–10.
16. J. Hernandez-Sandoval, G.H. Garza-Elizondo, A.M. Samuel, S. Valtiierra, and F.H. Samuel: *Mater. Des.*, 2014, vol. 58, pp. 89–101.
17. W. Kasprzak, D. Emadi, M. Sahoo, and M. Aniolek: *Mater. Sci. Forum*, 2009, vols. 618–619, pp. 595–600.

18. W. Kasprzak, D.L. Chen, and S.K. Shaha: *J. Mater. Eng. Perform.*, 2013, vol. 22, pp. 1838–47.
19. S.K. Shaha, F. Czerwinski, W. Kasprzak, and D.L. Chen: *J. Alloys Compd.*, 2014, vol. 593, pp. 290–99.
20. T. Gao, X. Zhu, Q. Sun, and X. Liu: *J. Alloys Compd.*, 2013, vol. 567, pp. 82–88.
21. S.K. Shaha, F. Czerwinski, W. Kasprzak, and D.L. Chen: *Mater. Des.*, 2014, vol. 59, pp. 352–58.
22. K.L. Sahoo and B.N. Pathak: *J. Mater. Process. Technol.*, 2009, vol. 209, pp. 798–804.
23. X.-G. Chen and M. Fortier: *J. Mater. Process. Technol.*, 2010, vol. 210, pp. 1780–86.
24. C. Booth-Morrison, Z. Mao, M. Diaz, D.C. Dunand, C. Wolverton, and D.N. Seidman: *Acta Mater.*, 2012, vol. 60, pp. 4740–52.
25. Y. Li, Y. Yang, Y. Wu, L. Wang, and X. Liu: *Mater. Sci. Eng. A*, 2010, vol. 527, pp. 7132–37.
26. Y. Li, Y. Yang, Y. Wu, Z. Wei, and X. Liu: *Mater. Sci. Eng. A*, 2011, vol. 528, pp. 4427–30.
27. J.H. Hollomon: *Trans. AIME*, 1945, vol. 162, pp. 268–90.
28. Y. Meng, J. Cui, Z. Zhao, and Y. Zuo: *J. Alloy. Compd.*, 2013, vol. 573, pp. 102–11.
29. T.V. Atamanenko, D.G. Eskin, M. Sluiter, and L. Katgerman: *J. Alloy. Compd.*, 2011, vol. 509, pp. 57–60.
30. T. Gao and X. Liu: *J. Mater. Sci. Technol.*, 2013, vol. 29, pp. 291–96.
31. J.A. Taylor: *Proc. Mater. Sci.*, 2012, vol. 1, pp. 19–33.
32. S.K. Shaha, F. Czerwinski, W. Kasprzak, J. Friedman, and D.L. Chen: *Int. J. Fatigue*, 2015, vol. 70, pp. 383–94.
33. O. Elsebaie, A.M. Samuel, F.H. Samuel, and H.W. Doty: *Mater. Des.*, 2014, vol. 60, pp. 496–509.
34. L.G. Hou, H. Cui, Y.H. Cai, and J.S. Zhang: *Mater. Sci. Eng. A*, 2009, vol. 527, pp. 85–92.
35. K.L. Fan, G.Q. He, X.S. Liu, B. Liu, M. She, Y.L. Yuan, Y. Yang, and Q. Lu: *Mater. Sci. Eng. A*, 2013, vols. 78–85, p. 586.
36. S.K. Shaha, F. Czerwinski, W. Kasprzak, J. Friedman, and D.L. Chen: *Thermochim. Acta*, 2014, vol. 595, pp. 11–16.
37. L. Hurtalová, E. Tillová, and M. Chalupová: *Arch. Mech. Eng.*, 2012, vol. 59, pp. 385–96.
38. A.M. Mohamed, F.H. Samuel, and S. Al-kahtani: *Mater. Sci. Eng. A*, 2013, vol. 577, pp. 64–72.
39. L. Lasa and J.M. Rodriguez-Ibabe: *J. Mater. Sci.*, 2004, vol. 39, pp. 1343–55.
40. M.F. Ibrahim, E. Samuel, A.M. Samuel, A.M. Al-Ahmari, and F.H. Samuel: *Mater. Des.*, 2011, vol. 32, pp. 2130–42.
41. W. Kasprzak, B.S. Amirkhiz, and M. Niewczas: *J. Alloys Compd.*, 2014, vol. 595, pp. 67–79.
42. A.M. Samuel, J. Gauthier, and F.H. Samuel: *Metall. Mater. Trans. A*, 1996, vol. 27A, pp. 1785–98.
43. M. Tiryakioğlu, J. Campbell, and N.D. Alexopoulos: *Metall. Mater. Trans. B*, 2009, vol. 40B, pp. 802–11.
44. U.F. Kocks and H. Mecking: *Prog. Mater Sci.*, 2003, vol. 48, pp. 171–273.
45. M.R. Daymond, C. Hartig, and H. Mecking: *Acta Mater.*, 2005, vol. 53, pp. 2805–13.
46. S.K. Shaha, F. Czerwinski, D.L. Chen, and W. Kasprzak: *Mater. Sci. Technol.*, 2015, vol. 31, pp. 63–72.
47. J. Kratochvil and M. Saxlová: *Phys. Scripta*, 1993, vol. T49, pp. 399–404.
48. H.A. Elhadari, H.A. Patel, D.L. Chen, and W. Kasprzak: *Mater. Sci. Eng. A*, 2011, vol. 528, pp. 8128–38.
49. N. Afrin, D.L. Chen, X. Cao, and M. Jahazi: *Scripta Mater.*, 2007, vol. 57, pp. 1004–07.
50. A.R. Emami, S. Begum, D.L. Chen, T. Skszek, X.P. Niu, Y. Zhang, and F. Gabbianelli: *Mater. Sci. Eng. A*, 2009, vol. 516, pp. 31–41.
51. P.A. Rometsch and G.B. Schaffer: *Mater. Sci. Eng. A*, 2002, vol. 325, pp. 424–34.
52. W.F. Hosford: *Mechanical Behavior of Materials*, Cambridge University Press, New York, 2005, pp. 279–307.
53. Q.G. Wang, D. Apelian, and D.A. Lados: *J. Light Met.*, 2001, vol. 1, pp. 85–97.
54. Q.G. Wang, D. Apelian, and D.A. Lados: *J. Light Met.*, 2001, vol. 1, pp. 73–84.
55. H.R. Ammar, A.M. Samuel, and F.H. Samuel: *Int. J. Fatigue*, 2008, vol. 30, pp. 1024–35.
56. Q.G. Wang, P.N. Crepeau, C.J. Davidson, and J.R. Griffiths: *Metall. Mater. Trans. B*, 2006, vol. 37, pp. 887–95.
57. J.Z. Zhou, S. Huang, J. Sheng, J.Z. Lu, C.D. Wang, K.M. Chen, H.Y. Ruan, and H.S. Chen: *Mater. Sci. Eng. A*, 2012, vol. 539, pp. 360–68.
58. J.B. Jordon, M.F. Horstemeyer, N. Yang, J.F. Major, K.A. Gall, J. Fan, and D.L. McDowell: *Metall. Mater. Trans. A*, 2010, vol. 41, pp. 356–63.
59. M.F. Ibrahim, E. Samuel, A.M. Samuel, A.M. Al-Ahmari, and F.H. Samuel: *Mater. Des.*, 2011, vol. 32, pp. 3900–10.
60. Y. Yang, K. Yu, Y. Li, D. Zhao, and X. Liu: *Mater. Des.*, 2012, vol. 33, pp. 220–25.
61. O. Reiso, H. Westengen, and L. Auran: *Internationale Leichtmetalltagung*, Montanuniv Leoben, Leoben, 1981.
62. M. Okayasu, R. Sato, S. Takasu, A. Niikura, and T. Shiraishi: *Mater. Sci. Eng. A*, 2012, vol. 534, pp. 614–23.